

Resonant sterile neutrino dark matter in the local and high- z Universe

Brandon Bozek,¹★ Michael Boylan-Kolchin,¹ Shunsaku Horiuchi,²
Shea Garrison-Kimmel,³ Kevork Abazajian⁴ and James S. Bullock⁴

¹Department of Astronomy, The University of Texas at Austin, 2515 Speedway, Stop C1400, Austin, TX 78712, USA

²Center for Neutrino Physics, Department of Physics, Virginia Tech, Blacksburg, VA 24061, USA

³TAPIR, California Institute of Technology, Pasadena, CA 91125, USA

⁴Department of Physics and Astronomy, University of California, Irvine, CA 92697, USA

Accepted 2016 March 21. Received 2016 March 19; in original form 2015 December 14

ABSTRACT

Sterile neutrinos comprise an entire class of dark matter models that, depending on their production mechanism, can be hot, warm, or cold dark matter (CDM). We simulate the Local Group and representative volumes of the Universe in a variety of sterile neutrino models, all of which are consistent with the possible existence of a radiative decay line at ~ 3.5 keV. We compare models of production via resonances in the presence of a lepton asymmetry (suggested by Shi & Fuller 1999) to ‘thermal’ models. We find that properties in the highly non-linear regime – e.g. counts of satellites and internal properties of haloes and subhaloes – are insensitive to the precise fall-off in power with wavenumber, indicating that non-linear evolution essentially washes away differences in the initial (linear) matter power spectrum. In the quasi-linear regime at higher redshifts, however, quantitative differences in the 3D matter power spectra remain, raising the possibility that such models can be tested with future observations of the Lyman- α forest. While many of the sterile neutrino models largely eliminate multiple small-scale issues within the CDM paradigm, we show that these models may be ruled out in the near future via discoveries of additional dwarf satellites in the Local Group.

Key words: Galaxy: halo – Local Group – cosmology: theory – dark matter – large-scale structure of Universe.

1 INTRODUCTION

The triumphs of the now-standard Λ cold dark matter (Λ CDM) model are manifold (see Frenk & White 2012; Primack 2015 for recent reviews). Nagging doubts about Λ CDM on small scales (corresponding to linear perturbations with masses of $\lesssim 10^{10} M_{\odot}$) have lingered, however, owing in large part to the difficulty of modelling low-mass perturbations from the linear to the non-linear regime. In studying the highly non-linear regime, a number of issues have arisen on these scales. In particular, several possible conflicts exist between theory and observations on the scale of dwarf galaxies ($M_{*} \lesssim 0.1 L^{*}$ or $M_{\text{halo}} \lesssim 10^{11} M_{\odot}$ at $z = 0$). These small-scale issues include: the overprediction of the abundance of low-mass dark matter (DM) haloes relative to the observed number of satellite galaxies in the Local Group (the missing satellites problem – Klypin et al. 1999; Moore et al. 1999), the prediction of a central cusp in the DM halo density profile while the density profile of dwarf galaxies inferred from observations favour a core (the core-cusp problem – Flores & Primack 1994; Moore 1994), and the

overprediction of the density in the subhaloes expected to host the bright, classical Milky Way (MW) dwarf galaxies [the ‘Too Big To Fail’ (TBTf) Problem – Boylan-Kolchin, Bullock & Kaplinghat 2011, 2012].

Within the CDM paradigm, the resolution to these issues must lie in the baryonic physics of galaxy formation. A combination of (global) photoionization and stellar feedback may suppress star formation below some mass threshold, which would resolve the missing satellites problem (Bullock, Kravtsov & Weinberg 2000; Kravtsov, Gnedin & Klypin 2004). Proposed resolutions of the Core-Cusp problem and the TBTf issue require supernova-driven gravitational potential fluctuations that remove substantial quantities of DM from the centre of DM haloes (possibly in concert with tidal stripping) to flatten cuspy density profiles into cores (Governato et al. 2010; Brook et al. 2011; Governato et al. 2012; Zolotov et al. 2012; Di Cintio et al. 2014; Oñorbe et al. 2015). There is some debate in the literature as to whether these solutions can be generally viable (Peñarrubia et al. 2012; Garrison-Kimmel et al. 2013). Lowering the mass of the MW provides a simple resolution to the TBTf problem (di Cintio et al. 2011; Wang et al. 2012; Vera-Ciro et al. 2013). However, considering together the total mass of the Local Group (van der Marel et al. 2012) and the TBTf problem

★E-mail: bozek@astro.as.utexas.edu

of Andromeda (M31), the TBTF problem will persist for at least one of the two massive Local Group galaxies (Tollerud et al. 2014). Moreover, the TBTF problem is also an issue for Local Group and field haloes, where stripping is unlikely to occur and host halo mass arguments do not apply (Garrison-Kimmel et al. 2014b; Kirby et al. 2014; Papastergis et al. 2015). The CDM small-scale issues extending beyond the virial radii of the MW and M31 galaxies underscore the importance of studying the Local Group as a whole.

These small-scale issues in CDM have led to a reconsideration of warm dark matter (WDM) models of structure formation. In WDM scenarios, DM has a cosmologically important free-streaming scale that erases primordial perturbations below a characteristic scale, one that is relevant for galaxy formation. For example, a ~ 2 keV DM particle produced in thermal equilibrium reduces power for (linear) wavenumbers larger than $k \sim 10 h \text{ Mpc}^{-1}$, corresponding to (linear) mass scales of $\sim 10^9 M_\odot$ (Bode, Ostriker & Turok 2001; Anderhalden et al. 2012, 2013; Schneider et al. 2012; Lovell et al. 2014). Modifying the abundance of haloes at this mass scale will result in observable differences in the counts of dwarf galaxies around the Local Group and in the field in the low- z Universe. There are other DM models that feature a variety of mechanisms for suppressing structure formation on similar mass scales to WDM, including: self-interacting DM (Vogelsberger, Zavala & Loeb 2012; Rocha et al. 2013), ultralight axions (Marsh & Silk 2014; Marsh & Pop 2015), decaying DM (Wang et al. 2014) and DM-relativistic species interactions (Bøhm et al. 2014; Buckley et al. 2014). We do not consider these models further, but instead focus on WDM in the form of sterile neutrinos.

keV-scale sterile neutrinos represent a plausible DM candidate from a particle physics point of view (Dodelson & Widrow 1994; Shi & Fuller 1999; Asaka, Blanchet & Shaposhnikov 2005; de Gouvêa 2005). The recent detection of a possible line at 3.55 keV in the Perseus cluster (Boyarsky et al. 2014; Bulbul et al. 2014), stacked galaxy clusters (Bulbul et al. 2014), the MW Galactic Center (Boyarsky et al. 2015), M31 (Boyarsky et al. 2014), and eight other clusters of galaxies at greater than 2σ (Iakubovskiy et al. 2015), while contentious, has further heightened interest in keV-scale DM: the radiative decay of a 7.1 keV sterile neutrino would result in a 3.55 keV X-ray line. If this is indeed the origin of the line, it is the first non-gravitational signature of DM and is revolutionary. However, even in this case, the effects of such a particle on structure formation are *not* uniquely determined by its mass: different production mechanisms produce different momentum–space distributions of the sterile neutrino DM for particles of identical mass.

WDM models have often been categorized in two types (e.g. Colombi, Dodelson & Widrow 1996). ‘Early decoupled species’ such as gravitinos, which are often referred to as ‘thermal’ WDM, are produced in thermal equilibrium but decouple early (at $T \gg 100 \text{ GeV}$); for such particles, the particle mass and decoupling temperature set the effect on large-scale structure. ‘Sterile neutrinos’ often is used to mean right-handed neutrinos produced by oscillations at $T \lesssim 1 \text{ GeV}$. So long as g_* is unchanged during their production (and in the absence of any resonant production), one can derive a mapping between early decoupled species (thermal WDM) and oscillation-produced sterile neutrino DM (Colombi et al. 1996; Viel et al. 2005):

$$m(\nu_s) = 4.43 \text{ keV} \left(\frac{m_{\text{thermal}}}{1 \text{ keV}} \right)^{4/3} \left(\frac{\Omega_{\text{DM}} h^2}{0.1225} \right)^{-1/3}. \quad (1)$$

In the well-known Dodelson–Widrow (1994) model of sterile neutrinos produced via non-resonant oscillations, however, g_* *does* change during oscillation production. This change is particularly large during the quark–hadron transition, which alters production

significantly (Abazajian & Fuller 2002). The applicability of equation (1) to cosmological interpretations of the effects of sterile neutrinos is therefore not clear, a priori. Abazajian (2006) calculated the effects of the change of g_* through the quark–hadron transition and the effects of the commensurate neutrino opacity change. This results in a correction between equivalent particle masses for thermal early decoupled WDM and non-resonant sterile neutrino WDM; the corrected relationship is given by

$$m(\nu_s) = 3.90 \text{ keV} \left(\frac{m_{\text{thermal}}}{1 \text{ keV}} \right)^{1.294} \left(\frac{\Omega_{\text{DM}} h^2}{0.1225} \right)^{-1/3}. \quad (2)$$

We have calculated this relation by matching the value of half-mode suppression between the non-resonant Dodelson–Widrow transfer functions calculated in Abazajian (2006) and the thermal WDM transfer functions, e.g. in Viel et al. (2005). Equation (2) is accurate in the half-mode match to within 1 per cent given the two transfer function relations. We note that while the difference in the normalization and exponent in the thermal mass term of equation (2) relative to equation (1) is small, this difference can have a significant (~ 20 per cent) effect on Dodelson–Widrow sterile neutrino mass constraints, particularly at larger particle masses that are currently being derived from constraints based on Lyman- α forest data (Baur et al. 2015). The cosmological effects of sterile neutrinos produced through early decoupling (e.g. Patwardhan et al. 2015) actually behave as thermal WDM in their transfer function and not as oscillation-produced transfer functions.

In the case of the Shi–Fuller (1999) sterile neutrino model of resonant production in the presence of a large lepton asymmetry, the momentum distributions are substantially non-thermal and their transfer functions need to be specifically calculated. The main effect of this non-thermal distribution is to modify the linear theory transfer function relative to thermal models. How this modification evolves in the non-linear regime is not obvious and must be studied with numerical simulations, in general. Furthermore, as shown by Abazajian (2014) and Venumadhav et al. (2015), a large range of different behaviours are possible for a Shi–Fuller sterile neutrino of a given mass, with the mixing angle between sterile and ordinary neutrinos and cosmological lepton number determining on which scales power is suppressed. Neither equation (1) nor equation (2) therefore applies to Shi–Fuller sterile neutrinos.

In this work, we explore a range of parameter space of the Shi–Fuller (resonantly produced) sterile neutrino DM model that can account for 3.55 keV X-ray observations; our goal is to study the effects of such models on cosmological structure formation. Previous studies of the MW in a WDM cosmology focus only on thermal WDM particle models (Lovell et al. 2012, 2014; Kennedy et al. 2014) or approximate resonant sterile neutrino DM with thermal WDM transfer functions (Bose et al. 2016). Approximations are used because calculating the exact transfer function for resonantly produced sterile neutrino models where particles are produced out of thermal equilibrium is challenging, and differences between thermal and resonant sterile neutrino transfer functions appear small. Here, as was done in a companion work (Horiuchi et al. 2016), we use sterile neutrino transfer functions based on detailed Boltzmann code calculations and evaluate the relevance of thermal WDM approximations used to place constraints on sterile neutrino model parameter space.

The focus of this paper is two-fold. First, we examine the properties of Local Group galaxies using zoom-in, dissipationless N -body simulations for a variety of WDM models in order to explore solutions to CDM small-scale issues and predict distinguishable features of a WDM Local Group. Secondly, we determine the relevance of thermal WDM approximations to resonant sterile neutrino

WDM models by comparing Local Group properties, DM halo mass functions in large cosmological volumes, and the 3D matter power spectrum at high redshift.

The paper is organized as follows. In Section 2, we describe the WDM models evaluated in this work, the numerical simulation details, and analysis methods. We present our results for the Local Group simulations in Section 3 and field halo velocity functions of cosmological volume simulations in Section 4. We give the high-redshift matter power spectrum results of the cosmological volume simulations in Section 5. In Section 6, we discuss our results and present our conclusions.

2 SIMULATIONS

Throughout this work, we consider Shi-Fuller resonantly produced sterile neutrino DM models with a particle mass of $m_\nu = 7.1$ keV that are consistent with the observed 3.55 keV line. As described in the Section 1, the particle mass does not uniquely specify the effect such a particle has on structure formation. We examine a range of sterile neutrino parameters that modify the linear matter power spectrum on scales relevant to small-scale structure formation. We additionally consider two calculations of Shi-Fuller models based on the work of Abazajian (2014, hereafter A14) and also the more recent results of Venumadhav (2015, hereafter V15).

The A14 models are parametrized by L , the lepton number of the Universe (relative to the photon number) prior to resonant production. We consider the models discussed in A14 of $L = 4.6 \times 10^{-4}$, 7×10^{-4} , and 8×10^{-4} (hereafter, L46, L7, and L8). These models bracket the region of parameter space that is consistent with producing the 3.55 keV line and suppresses the linear matter power spectrum on small scales that are relevant for DM halo counts, as it relates to the missing satellites problem. Once m_ν is fixed and the lepton number is specified, the mixing angle $\sin^2(2\theta)$ is also determined. The case of L7 has a mixing angle of $\sin^2(2\theta) \approx 3 \times 10^{-11}$, for example.

The models from V15 include a more complete treatment of the redistribution of lepton number and opacity of active neutrinos. We consider three V15 models parametrized by their mixing angles: $\sin^2(2\theta) = \{0.8, 2.9, \text{ and } 20\} \times 10^{-11}$ (hereafter, S208, S229, and S220). The V15 models are selected to bracket the region of sterile neutrino parameter space that is consistent with the candidate radiative decay line observations and have a similar half-mode suppression scale as the three A14 models. The lepton number (or equivalently here, the mixing angle) determines the resonantly produced sterile neutrino momentum distribution and therefore the suppression of the linear matter power spectrum. For example, the L7 and S229 have similar values of $\sin^2(2\theta)$. These models are therefore comparable through their suppression of the linear matter power spectrum. Fig. 1 shows the ‘relative’ transfer function, $T_{\text{rel}} = \sqrt{P_{\text{WDM}}/P_{\text{CDM}}}$, that describes the suppression of the linear matter power spectrum relative to CDM for these models. The T_{rel} of the L7 and S229 models in Fig. 1 show a similar degree of suppression relative to CDM down to large values of k where $T_{\text{rel}} > 0.1$, albeit with a slightly different shape.

Each relative transfer function can be fit by a comparable relative transfer function for a thermal WDM model, which we subsequently refer to as its ‘thermal equivalent’. The L7 and S229 cases have a thermal equivalent model of $m = 2$ keV (THM2), while the L46 (L8) thermal equivalent particle mass is larger (smaller). The effective ‘warmth’ of the sterile neutrino models is then represented by the scale where the linear matter power spectrum diverges from CDM matter power spectrum, where warmer models suppress power on

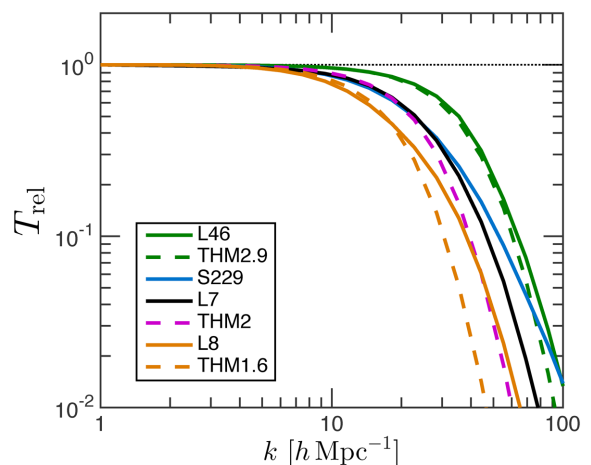


Figure 1. Suppression of the linear matter power spectrum of resonantly produced sterile neutrino models (solid lines) and their best-fitting thermal equivalent model (dashed lines) relative to CDM, where $T_{\text{rel}} = \sqrt{P_{\text{WDM}}/P_{\text{CDM}}}$. The L46 (solid; green), L7 (solid; black), and L8 (solid; orange) models are based on the sterile neutrino DM production calculations of Abazajian (2014), while S229 (solid; blue) model is based on the more accurate treatment of Venumadhav et al. (2015). The L7 and S229 models both share an equivalent thermal WDM model of $m = 2$ keV (THM2/dashed; magenta). The shape and large- k behaviour of the WDM transfer functions vary among the sterile neutrino models and compared with their thermal equivalent models.

larger scales. Importantly, despite representing the best-fitting case, the momentum distributions of the thermal equivalent models result in relative transfer functions that have different shapes from their sterile neutrino counterparts, as shown in Fig. 1. We explore this point in detail throughout this work.

The thermal equivalent transfer functions of our fiducial L7 and S229 models match closely at the half-mode scale ($k_{1/2}$), where $T_{\text{rel}}(k_{1/2}) = 0.5$, as is shown in Fig. 1. The half-mode scale indicates where free-streaming effects are significant, having suppressed the linear matter power spectrum by 50 per cent (Avila-Reese et al. 2001). The half-mode mass is defined as

$$M_{1/2} = \frac{4\pi}{3} \left(\frac{\lambda_{1/2}}{2} \right)^3 \bar{\rho}, \quad (3)$$

where $\lambda_{1/2} = 2\pi/k_{1/2}$.

We conduct two simulation suites. The first are a set of zoom-in, DM-only N -body simulations that are based on a single realization of a Local Group from the Exploring the Local Volume In Simulations (ELVIS) suite (Garrison-Kimmel et al. 2014a). The ELVIS suite is a series of high-resolution N -body simulations of 48 MW-sized DM haloes (24 in Local Group-like pairs, 24 isolated haloes) in a Λ CDM cosmology. The paired haloes are selected to be representative of the Local Group by resembling the MW and M31 in mass, separation, relative kinematics, and their ~ 2 Mpc scale environment. The ‘Thelma and Louise’ Local Group from the ELVIS suite was chosen to be the representative Local Volume targeted in this work. The Local Group zoom-in simulations are run for four of the sterile neutrino WDM models discussed above (L46, L7, L8, and S229) and a thermal $m = 2$ keV WDM model. These simulations are compared to the original CDM simulation from the ELVIS suite. The three A14 models are selected to bracket a range of linear matter power suppression, as shown in Fig. 1, that is predicted to resolve the missing satellites problem. The S229 and THM2 models, as discussed above, are directly comparable to the L7 model

Table 1. WDM models. Column 1: model label; Column 2: physical parameter that defines the model: cosmological lepton number (L), mixing angle between sterile and active neutrinos ($\sin^2(2\theta)$), or thermal WDM particle mass (m); Column 3: half-mode mass; Column 4: was a Local Group pair simulated for this model?; Column 5: final redshift of the cosmological volume simulation.

Model	Physical parameter	$M_{1/2} (h^{-1} M_{\odot})$	Local Group pair	z_f
L46	$L = 4.6 \times 10^{-4}$	2.1×10^8	Yes	2
THM2.9	$m = 2.9 \text{ keV}$	2.4×10^8	No	2
S220	$\sin^2(2\theta) = 20 \times 10^{-11}$	2.2×10^8	No	2
L7	$L = 7 \times 10^{-4}$	7.8×10^8	Yes	0
THM2	$m = 2 \text{ keV}$	9.4×10^8	Yes	0
S229	$\sin^2(2\theta) = 2.9 \times 10^{-11}$	8.2×10^8	Yes	0
L8	$L = 8 \times 10^{-4}$	2.1×10^9	Yes	2
THM1.6	$m = 1.6 \text{ keV}$	1.8×10^9	No	2
S208	$\sin^2(2\theta) = 0.8 \times 10^{-11}$	1.9×10^9	No	2

and facilitate an exploration of the relative transfer function shape on Local Group properties.¹

The Tree-PM N -body code GADGET-3, an updated version of the public GADGET-2 code (Springel 2005), was used to perform the simulations, which assume a WMAP7 cosmology: $\Omega_m = 0.266$, $\sigma_8 = 0.801$, $\Omega_{\Lambda} = 0.734$, $n_s = 0.963$, and $h = 0.71$ (Larson et al. 2011). The particle mass of the high-resolution zoom-in region is $m_p = 1.3 \times 10^5 h^{-1} M_{\odot}$, which gives an effective resolution of 4096^3 for the high-resolution region. The simulations start at an initial redshift of $z_i = 125$ and employ a Plummer-equivalent softening of $\epsilon = 1 h^{-1} \text{ kpc}$, which is constant in comoving units until $z = 9$, where it becomes fixed at $\epsilon = 100 h^{-1} \text{ pc}$ (physical) to redshift zero. The initial conditions for the simulation were set-up using the MUSIC code (Hahn & Abel 2011).

We do not include the relic velocity distribution of the WDM particles in the initial conditions of our simulations. The largest thermal root-mean-square velocity of the WDM models we consider here is $\sim 2 \text{ km s}^{-1}$ at the start of our simulations. This is a small fraction of the typical Zel'dovich velocities, $\sim 30 \text{ km s}^{-1}$, at that time. The contribution of the late-time thermal velocity distributions will then be negligible down to the resolution limit of our simulations (Avila-Reese et al. 2001; Colín, Valenzuela & Avila-Reese 2008; Boyarsky et al. 2009; Lovell et al. 2012; Macciò et al. 2012; Viel et al. 2012; Shao et al. 2013). The effects of free-streaming resulting from the large particle velocities in the early Universe are well described by the shape of the relative transfer function cutoffs alone.

Our second suite of simulations are homogeneously resolved, cosmological volume DM-only simulations of $N_p = 512^3$ particles in cubic volumes of box length $L = 25 h^{-1} \text{ Mpc}$ with a WMAP7 cosmology. We simulate the A14 (L46, L7, L8) and V15 (S220, S229, S208) sterile neutrino WDM models and their best-fitting thermal WDM models ($m = 1.6, 2, \text{ and } 2.9 \text{ keV}$; hereafter, THM1.6, THM2, and THM2.9). The Plummer-equivalent force softening for these simulations, $\epsilon = 1.25 h^{-1} \text{ kpc}$, is constant in comoving units for the duration of the simulation. The simulations start at $z_i = 125$. The L7, THM2, S229, and CDM simulations were evolved to $z = 0$; the L46, L8, S208, and S220 models were simulated to understand halo properties at high redshift and were therefore terminated at

$z = 2$. Table 1 lists the simulations conducted for each WDM model, the physical parameter that defines each WDM model, and the final redshift of each homogeneously resolved simulation. The non-linear matter power spectrum of each simulation was calculated using the PROCORR code (Obreschkow et al. 2013).

We use the Amiga Halo Finder (AHF; Knollmann & Knebe 2009) to identify self-bound dark matter haloes. The virial mass of a DM halo, M_{vir} , is defined as the mass contained within a sphere out to the virial radius, R_{vir} , within which the average density is 200 times the mean density of the Universe. We define R_{max} as the radius where the maximum velocity, V_{max} , of the circular velocity profile, $V_c(r) = \sqrt{GM(<r)}/r$, is reached for a DM halo at redshift zero. The assembly histories of the DM haloes are determined by the MERGERTREE code that is included in AHF. The maximum circular velocity of a DM halo over its entire assembly history is defined as V_{peak} . Halo partners across different simulations are also identified using the AHF MERGERTREE code by finding the corresponding halo that shares the most particles with the same GADGET-3 Particle IDs. For example, Halo A in the CDM simulation is considered a partner halo of Halo B in the L7 WDM simulation if both haloes maximize the function $N_{\text{AB}}^2/(N_{\text{A}}N_{\text{B}})$, where N_{AB} is the number of shared particles in each halo, N_{A} is the number of particles in halo A, and N_{B} is the number of particles in halo B. This criterion is determined for haloes in each simulation type with respect to every other simulation type and then compared for overlap between simulation types. When comparing haloes directly across different simulation types, we do not include haloes that fail this criterion, even if the haloes satisfy a separate selection criteria (such as a range of halo masses).

The formation of haloes below the free-streaming scale in WDM should be highly suppressed; however, WDM numerical simulations find an excess of low-mass haloes compared to expectations both from theory and in comparison to CDM, where the CDM linear matter power spectrum has significantly more power than WDM. These haloes in WDM are numerical artefacts resulting from fragmentation of filaments induced by discreteness noise and exist whether the initial particle load is grid-based or glass-based (Wang & White 2007). Two methods that address this issue of spurious haloes are: removing haloes below a limiting mass and shape criterion (Lovell et al. 2014; Schneider 2015), or considering only haloes with a mass far above the mass scale where spurious halo formation is a significant problem. In this work, we take the latter approach.

We note, however, that the contamination from spurious haloes is likely to be small even at the resolution limit of our Local Group simulation ($V_{\text{max}} > 8 \text{ km s}^{-1}$). Fig. 2 shows the relationship of the peak mass, M_{peak} , to $V_{\text{max}}(z = 0)$ of Local Group field haloes in the

¹ A related work by Horiuchi et al. (2016) compares zoom-in simulations of an isolated MW-sized DM halo for the V15 models S208, S229, and S220 with observations of the Local Group satellites specifically to determine sterile neutrino model resolutions to the missing satellites and TBTF problems.

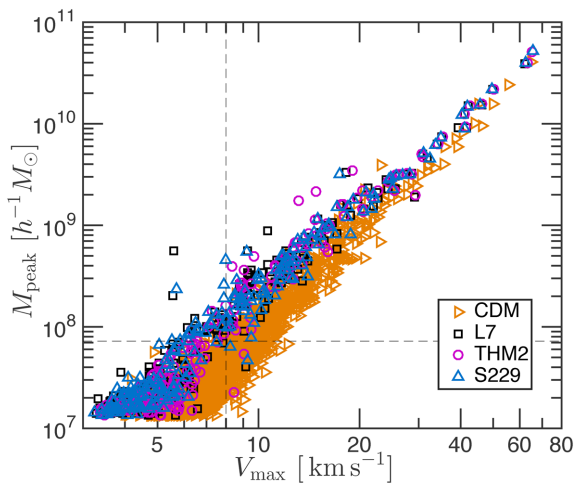


Figure 2. The peak mass of CDM and WDM Local Group field haloes with respect to V_{\max} at $z = 0$. For a fixed peak mass bin, the WDM haloes have a smaller V_{\max} value, indicating a lower central density. The three WDM models shown here (L7, THM2, and S229) have the same half-mode suppression scale. Their Local Group field halo sets shown here have a similar distribution in $M_{\text{peak}} - V_{\max}$ space. The vertical dashed-line shows the convergence limit of the simulation of $V_{\max} = 8 \text{ km s}^{-1}$ and the horizontal dashed-line gives the limiting mass M_{lim} as defined by Lovell et al. (2014), below which the haloes may have formed via artificial fragmentation. Only a few points fall in the bottom-right section as delineated by the dashed lines, indicating that our results are robust against discreteness effects.

CDM, L7, S229, and THM2 simulations. The vertical and horizontal dashed lines show the resolution limit at $V_{\max} = 8 \text{ km s}^{-1}$ and the limiting mass, defined as $M_{\text{lim}} = 10.1 \bar{\rho} d k_{\text{peak}}^{-2}$ (Wang & White 2007), respectively. We follow Lovell et al. (2014) and multiply this value by $\kappa = 0.5$ in order to best account for the mass scale below which artificial fragmentation dominates to obtain a value of $M_{\text{lim}} = 7.25 \times 10^7 M_{\odot} h^{-1}$. Haloes in the bottom-right quadrant of Fig. 2 are haloes that are above our resolution limit, but below the limiting mass, where their formation may have been the result of artificial fragmentation. The small number of points in this section of the figure illustrates that our results are not strongly contaminated by artificial fragmentation. However, when considering the internal properties of DM haloes, we base our conclusions on haloes with $V_{\max} > 15 \text{ km s}^{-1}$, which we define as our ‘artificial fragmentation limit’. This is a very conservative choice that selects haloes with an M_{peak} value significantly above M_{lim} , as shown in Fig. 2. We quote results for haloes with $V_{\max} > 8 \text{ km s}^{-1}$ where appropriate.²

3 THE LOCAL GROUP

3.1 Local Group host haloes

The general properties of the Thelma and Louise host haloes at redshift zero (e.g. the virial mass, virial radius, physical separation) are similar for each DM model considered here. The values for these halo properties (among others) can be found in Table 2 for each DM model. The general make-up of the host haloes are unaffected by the relative warmth of the respective WDM models.

² A few haloes in Fig. 2 have a M_{peak} value scattered above the general trend exhibited by the majority of haloes. These haloes experienced mass-loss from an encounter with another halo at some time in their history.

The spherically averaged density profiles and ratios of the WDM to CDM density profiles for the Thelma and Louise host haloes at $z = 0$ are shown in Fig. 3. The density profiles for each host show good agreement for all DM models at all radii. The ratios of the WDM and CDM hosts’ density profiles show only small departures from unity on most scales. The larger variations near the virial radius in the Louise DM density profiles are due to variations in the radial distribution of large substructures. Inside the resolution limit of $r = 1 h^{-1} \text{ kpc}$, the density ratios show strong fluctuations that are likely the result of numerical effects.

We have also investigated the shape of both host haloes in the CDM, L7, THM2, and S229 models by comparing the ratios of the minor and intermediate halo axes relative to the major halo axis. The host haloes shapes are triaxial at all radii with some variation in shape with radius. The DM model type does not affect the host halo shape as there are no significant differences in the Thelma and Louise axis ratios at any radius between CDM and WDM models.

The mass assembly histories of the host haloes for each DM model are shown in Fig. 4. After a redshift of $z = 5$, both host halo assembly histories are identical for all DM models. Prior to $z = 5$, the hosts’ assembly histories diverge for each DM model. Although the WDM model hosts collapse later than in the CDM model, there is not a correlation between the WDM model warmth and the initial collapse time nor with the subsequent mass build-up leading up to the common assembly history of $z < 5$. The host halo mass for each WDM model at the time of initial collapse is near or below the half-mode mass, $M_{1/2}$, (as listed in Table 1) where free-streaming effects that suppress structure formation are significant. The early mass assembly of the host haloes are then likely built up from the merging of haloes with masses on the order of $M_{1/2}$. The model-dependent nature of this mass scale then accounts for the differences in the initial collapse times and early mass assembly history of the different DM model host haloes shown in Fig. 4.

3.2 Local Group halo abundances

The cumulative V_{\max} functions for Thelma and Louise subhaloes, Local Group field haloes (located within 1.2 Mpc of either host centre, but outside both host virial radii), and a Local Volume set (all DM haloes within 1.2 Mpc of either host centre) are shown in Fig. 5. The CDM model predicts hundreds of subhaloes within each host’s virial radius and thousands in the Local Group down to the resolution limit of $V_{\max} \geq 8 \text{ km s}^{-1}$. The Thelma, Louise, Local Group field, and Local Volume cumulative V_{\max} functions for the WDM models are reduced relative to the CDM cumulative V_{\max} function at all masses to a degree that depends on the warmth of the model; warmer models have a lesser number of subhaloes relative to CDM. The relative suppression in the WDM cumulative V_{\max} functions is more pronounced at the low-mass end where the strong suppression in the small-scale power of the transfer functions in Fig. 1 results in greatly reduced low-mass halo formation. For example, the L7 model cumulative V_{\max} functions are reduced by a factor of 10 relative to CDM at the resolution limit, even without removing artificial subhaloes.

The cumulative subhalo V_{\max} functions of both host haloes show a strong similarity between L7 and S229 sterile neutrino models and their thermal equivalent $m = 2 \text{ keV}$ WDM model over the full V_{\max} range. There are small differences, of the order of 10–20 per cent, between the sterile neutrino and thermal equivalent models’ low-mass subhalo abundances near the resolution limit. The Local Group and Local Volume V_{\max} functions also find a slightly greater number of low-mass DM haloes (~ 20 per cent) for the sterile neutrino models

Table 2. Host halo properties. Column 1: model label; Column 2: host halo virial mass; Column 3: virial radius; Column 4: maximum circular velocity; Column 5: radius of circular velocity maximum; Column 6: separation between host haloes; Column 7: number of haloes above resolution limit; Column 8: number of haloes above the artificial fragmentation limit.

Model	M_{vir} ($h^{-1} M_{\odot}$)	R_{vir} ($h^{-1} M_{\odot}$)	V_{max} (km s^{-1})	R_{max} ($h^{-1} \text{kpc}$)	Δ ($h^{-1} \text{kpc}$)	$N(>8 \text{ km s}^{-1})$	$N(>15 \text{ km s}^{-1})$
CDM (Thelma)	1.05×10^{12}	256.69	171.48	61.69	623.7114	468	69
CDM (Louise)	8.50×10^{11}	239.52	158.82	33.07	623.7114	463	70
L46 (Thelma)	1.04×10^{12}	256.44	172.08	60.21	657.6297	101	38
L46 (Louise)	8.50×10^{11}	239.56	156.83	29.74	657.6297	106	37
L7 (Thelma)	1.04×10^{12}	256.30	171.03	60.81	665.3431	55	23
L7 (Louise)	8.47×10^{11}	239.22	153.69	25.26	665.3431	53	18
THM2 (Thelma)	1.05×10^{12}	256.76	170.99	61.23	663.9513	48	26
THM2 (Louise)	8.44×10^{11}	238.96	155.72	26.18	663.9513	48	17
S229 (Thelma)	1.05×10^{12}	256.62	170.89	65.4	661.1437	59	26
S229 (Louise)	8.49×10^{11}	239.39	154.65	25.36	661.1437	56	19
L8 (Thelma)	1.05×10^{12}	256.71	171.63	62.97	662.5239	36	21
L8 (Louise)	8.43×10^{11}	238.88	156.51	25.22	662.5239	30	11

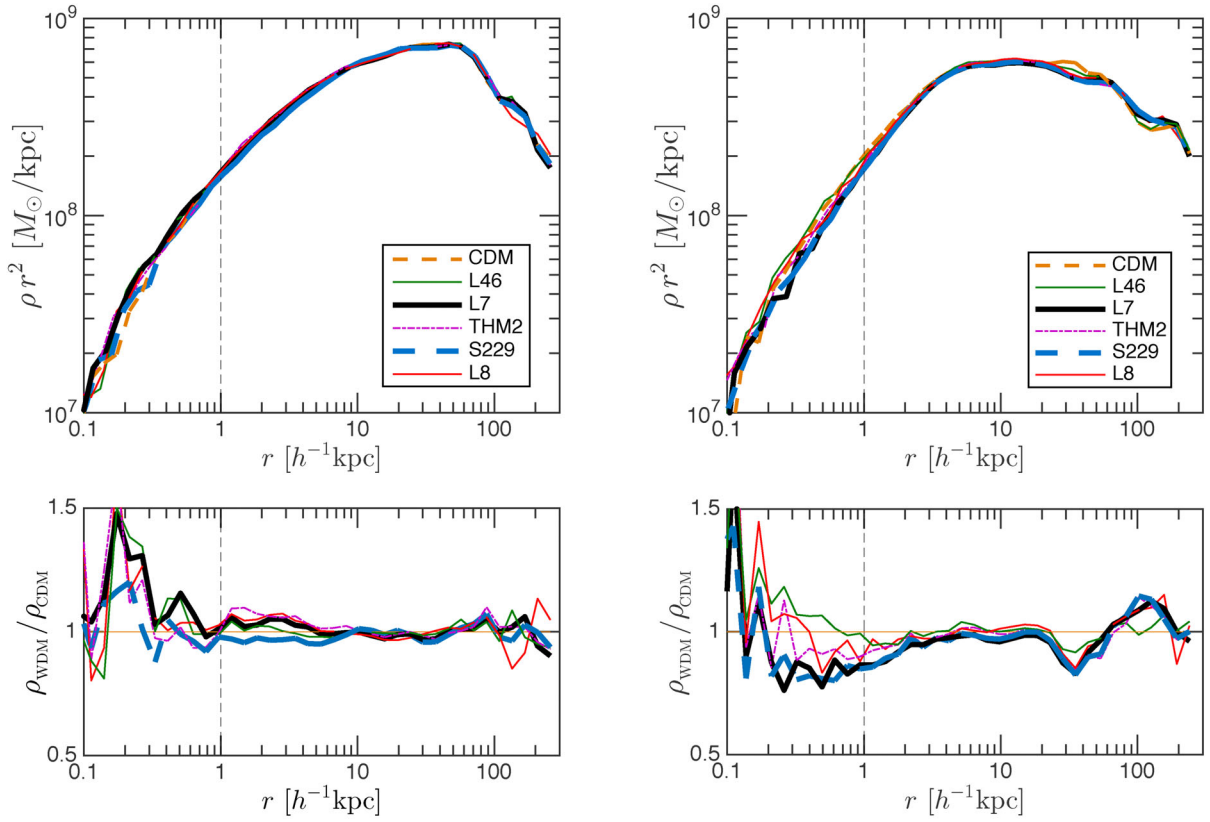


Figure 3. The density profiles (top row) and ratio of WDM and CDM density profiles (bottom row) of host haloes Thelma (left-hand column) and Louise (right-hand column) for the CDM (orange; dashed) and WDM models: L7 (black; thick-solid), THM2 (magenta; dot-dashed), L46 (green; thin-solid), L8 (red; thin-solid), S229 (blue; dashed). The dashed-vertical line marks the largest convergence radius ($r = 1 h^{-1} \text{kpc}$) based on the criterion of Power et al. (2003) as determined by the AHF halo finder (Knollmann & Knebe 2009). Differences for $r < 1 h^{-1} \text{kpc}$ are likely due to lack of numerical convergence. The density profiles for each model are very similar over the full radial range of each host. Small variations in the outer density profiles come from individual massive substructures.

than their thermal equivalent model. We caution, however, that these differences are not only near the resolution limit of the simulations, but also set in for $V_{\text{max}} < 15 \text{ km s}^{-1}$, where artificial fragmentation may remain an issue. The relevance of this difference in the low-mass halo abundance as it relates to satellite galaxy counts in the MW and M31 are discussed in detail by Horiuchi et al. (2016).

Fig. 6 illustrates the relationship between the half-mode mass ($M_{1/2}$), the halo mass scale where free-streaming effects are significant, and the total number of haloes in the V_{max} function above a cutoff velocity. We consider the total number of haloes above the cuts of $V_{\text{max}} \geq 8 \text{ km s}^{-1}$ and $V_{\text{max}} \geq 15 \text{ km s}^{-1}$. We fit the points in each panel of Fig. 6 to a power-law relation, $y \propto x^p$, where

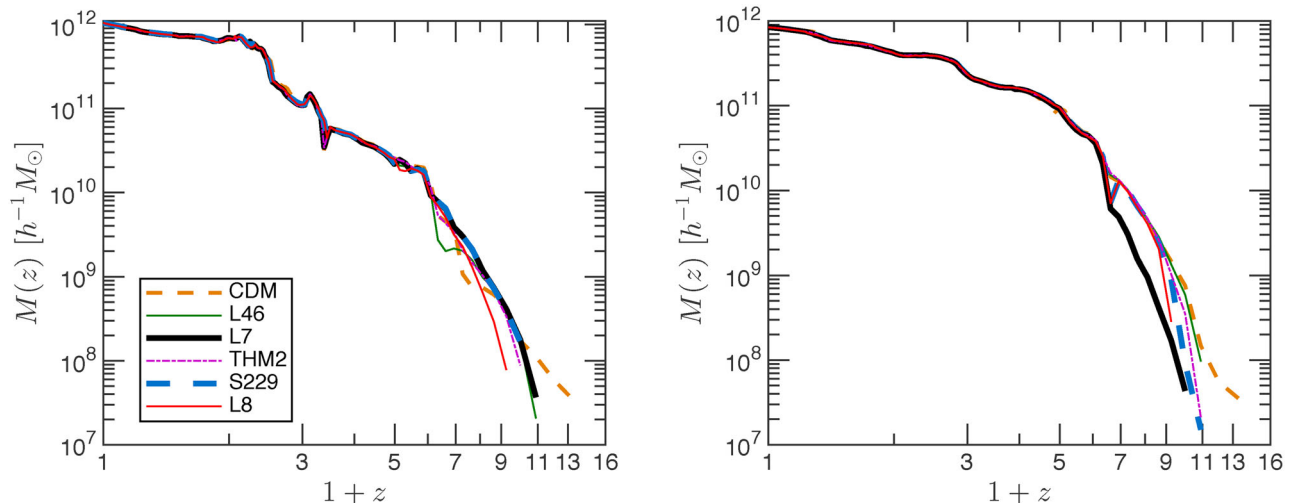


Figure 4. The mass assembly histories of host haloes Thelma (left-hand panel) and Louise (right-hand panel) for the DM models: L7 (black; thick-solid), THM2 (magenta; dot-dashed), L4.6 (green; thin-solid), L8 (red; thin-solid), S229 (blue; dashed), CDM (orange; dashed). After a redshift of $z = 5$, the virial mass evolution of each halo is identical for each DM model. Prior to $z = 5$, there are small departures from a common assembly history that are not correlated with WDM model warmth. The host halo masses at initial collapse are near (or below) the half-mode mass of each WDM model (listed in Table 1). The random departures from the early common assembly history are likely related to the mass build-up of haloes near the different models’ half-mode scales, where free-streaming effects are relevant.

$n = -0.40$ (-0.51) for the subhalo sets of Thelma and Louise for $V_{\max} > 15$ (8) km s^{-1} , and $n = -0.40$ (-0.53) for the field haloes in the Local Group.

The half-mode mass is strongly predictive of the total number of subhaloes in both hosts (left-hand panel) and in the Local Group (right-hand panel) for both V_{\max} cuts. The subhalo mass function dependence on the filtering mass was previously studied in Dunstan et al. (2011) for non-resonant WDM models. The power-law trends of the host subhalo sets and the Local Group field haloes are very similar. Warmer WDM models show a larger dispersion around the power-law fit for Thelma and Louise subhalo abundances. This is likely due to the small number of subhaloes in the warmer models, since the variation around the trend is stronger for the larger V_{\max} cut and the trend in the Local Group for the larger V_{\max} cut is the same as the subhalo set. The slight difference in the half-mode mass between thermal and sterile neutrino models results in a small difference in the total number of haloes near the resolution limit in each host and in the Local Group.

3.3 Local Group subhalo and field halo internal structure

We next consider the internal structure of the Local Group field haloes and Thelma and Louise subhaloes. The rotation curves and density profile ratios of WDM haloes relative to CDM haloes for the S229, L7, and THM2 Local Group field haloes are shown in Fig. 7. We also determine the median rotation curves and median density profile ratios for each DM model halo set (thick, dark curves). For simplicity, the individual L7 halo curves are not shown (although the median values of the L7 sets are presented). The halo sets were selected by, first, identifying all CDM Local Group field haloes (located within 1.2 Mpc of either host centre, but outside both host virial radii). CDM Local Group field haloes are then divided into two mass bins: haloes with $V_{\max} > 25 \text{ km s}^{-1}$ (left-column panels) and $15 < V_{\max} < 25 \text{ km s}^{-1}$ (right-column panels). We then identify WDM Local Group field halo counterparts to these CDM haloes that satisfy the halo correlation criterion described in Section 2.

The WDM halo counterparts are required to also be located in the Local Group field, but not to follow the V_{\max} cuts given above, i.e. a WDM halo counterpart could be significantly more or less massive than the corresponding CDM halo. The THM2 and S229 WDM model rotation and density ratio curves, shown in Fig. 7, are solid for haloes with $V_{\max} > 15 \text{ km s}^{-1}$ and dashed for haloes with $8 < V_{\max} < 15 \text{ km s}^{-1}$. The CDM field haloes with $V_{\max} > 25 \text{ km s}^{-1}$ (left-hand column) have all WDM halo counterparts with $V_{\max} > 15 \text{ km s}^{-1}$. For CDM field haloes with $15 < V_{\max} < 25 \text{ km s}^{-1}$ (right-hand column), however, only a handful of WDM halo counterparts have a $V_{\max} > 15 \text{ km s}^{-1}$; most have a V_{\max} value of $8 < V_{\max} < 15 \text{ km s}^{-1}$. Since the majority of WDM counterparts to the CDM field haloes with $15 < V_{\max} < 25 \text{ km s}^{-1}$ have a V_{\max} value below the artificial fragmentation limit, we plot the median rotation curve and median density profile ratio for WDM counterparts with $V_{\max} > 15 \text{ km s}^{-1}$ (thick, solid curves) and for WDM haloes with $V_{\max} > 8 \text{ km s}^{-1}$ (thick, dashed curves) in the right-hand column panels of Fig. 7. While the WDM halo sets with $V_{\max} > 8 \text{ km s}^{-1}$ are possibly contaminated by artificial fragmentation, they represent the majority of WDM counterparts to the CDM field haloes in the low-mass bin. If artificial fragmentation is not significant, then the WDM field haloes with $V_{\max} > 8 \text{ km s}^{-1}$ are the appropriate comparisons to CDM field haloes with $15 < V_{\max} < 25 \text{ km s}^{-1}$. There is also a significant fraction of WDM counterpart haloes to CDM field haloes with $15 < V_{\max} < 25 \text{ km s}^{-1}$ that have a V_{\max} below our resolution limit, $V_{\max} < 8 \text{ km s}^{-1}$ (not shown). We do include these haloes in the subsequent analysis.

The median rotation curves of the L7, THM2 and S229 WDM models, shown in the top row panels of Fig. 7, fall uniformly below the CDM rotation curves for both V_{\max} sets. The reduction in the median WDM rotation curves relative to CDM is more pronounced in the lower mass halo sets (top-right panel) for the WDM haloes with $V_{\max} > 8 \text{ km s}^{-1}$. The median rotation curves of the L7, S229, and THM2 WDM models are similar for both V_{\max} sets, indicating that each WDM model has, on average, a similar reduction in the central density of their DM halo relative to CDM.

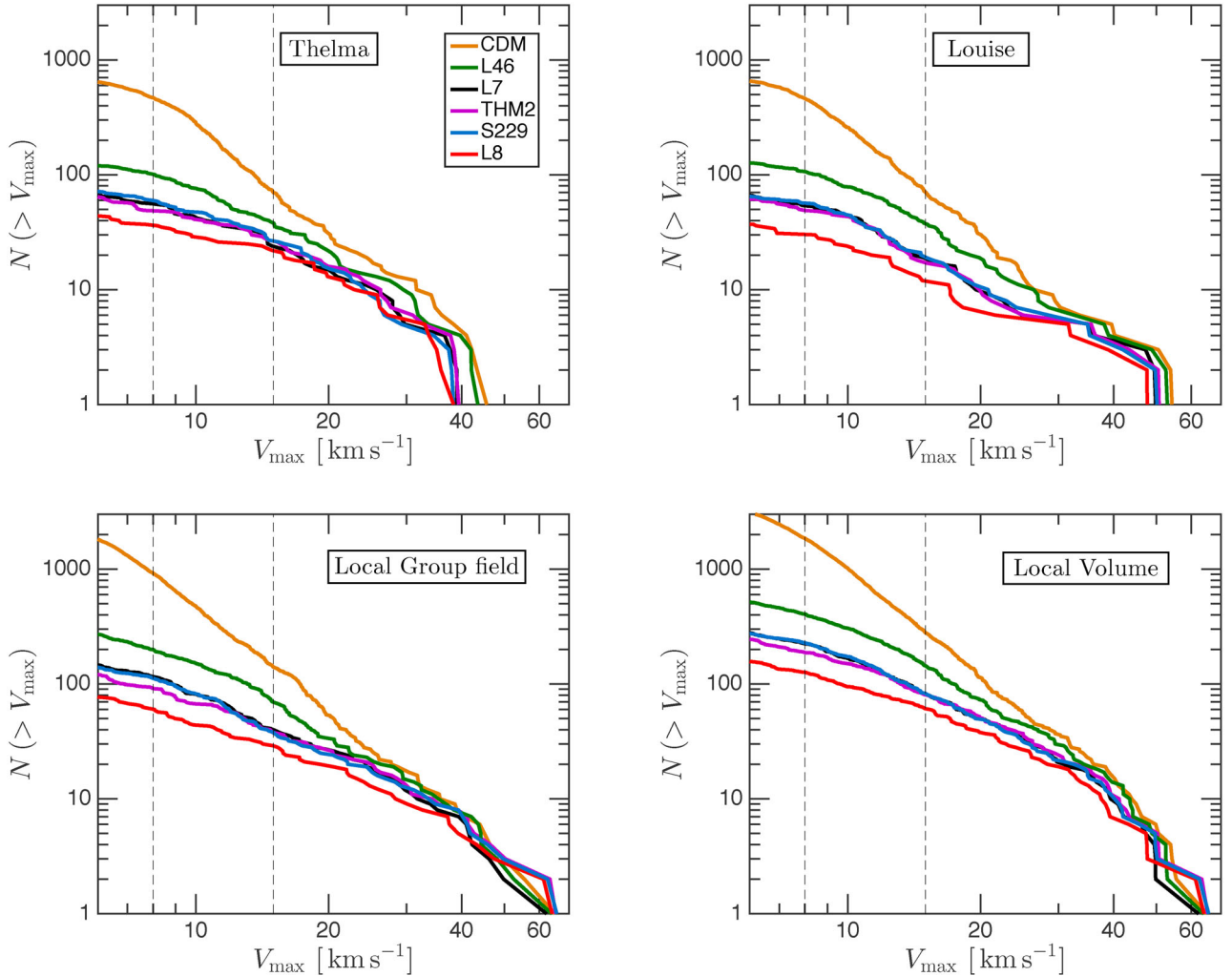


Figure 5. The cumulative subhalo V_{\max} function for hosts Thelma (top-left panel) and Louise (top-right panel), the Local Group field haloes (bottom-left panel), and all Local Volume haloes including host subhaloes and field haloes (bottom-right panel) for each DM model. The convergence limit of $V_{\max} = 8 \text{ km s}^{-1}$ and artificial fragmentation limit of $V_{\max} = 15 \text{ km s}^{-1}$ are, respectively, represented by the dashed-vertical lines. The five WDM models suppress the number of subhaloes at each mass relative to CDM.

The bottom panels of Fig. 7 show the ratio of the WDM field halo density profiles to CDM. The median density ratios of the Local Group WDM field halo counterparts to CDM field haloes with $V_{\max} > 25 \text{ km s}^{-1}$ (bottom-left panel) show that the CDM and WDM density profiles converge in the outer halo near $r = 20 h^{-1} \text{ kpc}$. The inner region of WDM density profiles reach an average reduction of ~ 40 per cent at $r \leq 1 h^{-1} \text{ kpc}$. For CDM field haloes with $15 < V_{\max} < 25 \text{ km s}^{-1}$, the median density ratios of the corresponding Local Group WDM field halo sets (bottom-right panel) show the WDM haloes with $V_{\max} > 15 \text{ km s}^{-1}$ are less dense than their CDM counterparts throughout, and are on average ~ 60 per cent less dense at $r = 1 h^{-1} \text{ kpc}$. Including the WDM field haloes with $V_{\max} > 8 \text{ km s}^{-1}$ in the comparison lowers the median density ratio an additional 10 per cent in the central $r \leq 1 h^{-1} \text{ kpc}$ and an additional 20 per cent at $r = 10 h^{-1} \text{ kpc}$ near the average halo virial radius. The median density ratios of the L7, S229, and THM2 WDM models are quantitatively similar at all radii for both V_{\max} sets and independent of the limiting WDM halo mass.

The reduction in the WDM central density is related to later formation times of WDM haloes relative to CDM haloes, which collapse earlier when the background matter density of the Universe

is greater. For both V_{\max} sets, there is considerable scatter in the individual halo density ratios at all radii. This spread in internal density ratios is reflected in the WDM rotation curves of both mass sets in the top panels. The CDM rotation curves are tightly clustered around the median, while the WDM sets show a larger degree of scatter. We find that, for an individual CDM halo, it is difficult to predict the exact amount of reduction in the corresponding WDM halo density profile (and likewise the rotation curve), however, in general, the less massive the CDM field halo the greater the reduction in the density profile (rotation curve) at all radii.

The internal properties of the WDM subhaloes of the Thelma and Louise host haloes are also significantly different than their CDM counterparts. We follow the same selection process for the host subhaloes sets, with the exception that the CDM subhaloes and their WDM counterparts are required to be within the virial radius of either host. For the $V_{\max} > 25 \text{ km s}^{-1}$ subhalo sets, shown in the left-hand column of Fig. 8, the median rotation curves and median density profile ratios of each DM model are quantitatively similar to the median values of the $V_{\max} > 25 \text{ km s}^{-1}$ Local Group field haloes. The L7, S229, and THM2 WDM models each have a ~ 40 per cent reduction at $r \leq 1 h^{-1} \text{ kpc}$ in the median density ratios

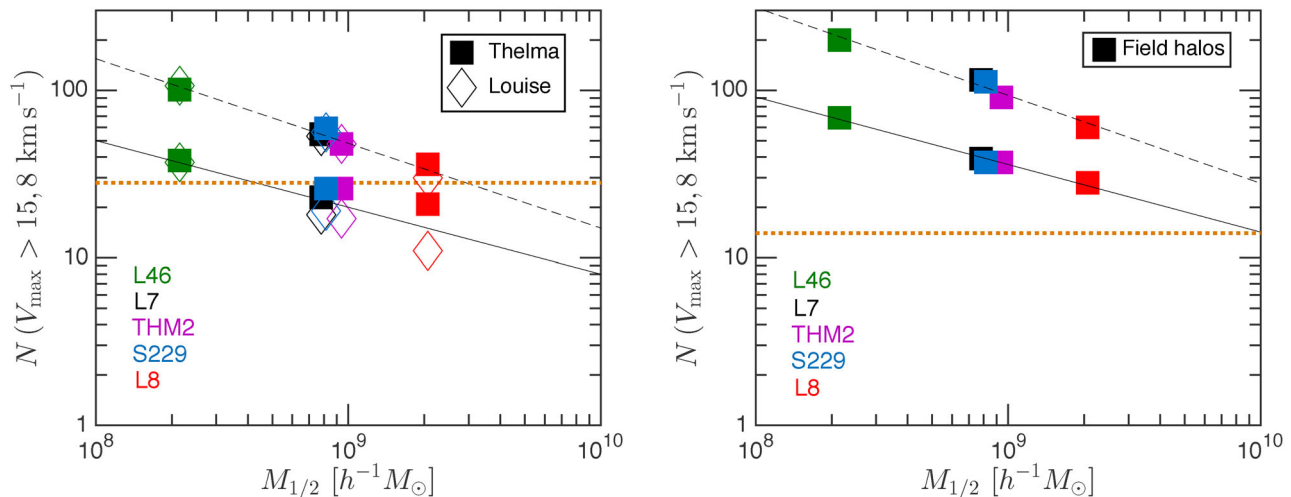


Figure 6. The cumulative number of subhaloes above a cutoff velocity in the cumulative subhalo V_{\max} functions for hosts Louise and Thelma (left-hand panel) and the Local Group field haloes (right-hand panel) with respect to the half-mode mass (defined in the text and listed in Table 1). In the left-hand panel, the solid squares (opened diamonds) represent Thelma (Louise) subhalo abundances for DM models: L7 (black), THM2 (magenta), L4.6 (green), L8 (red), and S229 (blue). The solid (dashed) black line gives the power-law fit for a cut of $V_{\max} = 15$ (8) km s^{-1} . The number of DM subhaloes in each host halo and in the Local Group field is well predicted by the half-mode mass of the relative transfer functions. The orange, dotted horizontal lines show the count of MW satellite galaxies (left; Horiuchi et al. 2016) and Local Group field galaxies (right; McConnachie 2012). The L8 model is in tension with the current count of MW satellite galaxies.

and a $\sim 5 \text{ km s}^{-1}$ drop in the median WDM rotation curves relative to the median CDM rotation curve, just as we found for the Local Group field haloes. We find no significant difference in the L7, S229, and THM2 model median rotation curves or density profile ratios.

The median rotation curve of CDM subhaloes with $15 \text{ km s}^{-1} < V_{\max} < 25 \text{ km s}^{-1}$ is also similar to the CDM Local Group field halo median rotation curve. The median rotation curves of the WDM subhalo counterparts with $V_{\max} > 15 \text{ km s}^{-1}$ (shown in the top-right panel of Fig. 8), however, have only a few km s^{-1} reduction in magnitude relative to CDM. The median density ratios of the WDM subhaloes with $V_{\max} > 15 \text{ km s}^{-1}$ show only a 40 per cent reduction in the central density relative to CDM. This is a smaller decrease than was found for WDM Local Group field haloes of the same V_{\max} cut. There is considerable scatter around the median for the individual density profile ratios of the WDM subhaloes with $V_{\max} > 15 \text{ km s}^{-1}$ that is likely due to tidal stripping effects in both the CDM and WDM subhaloes. Including the WDM subhaloes with $V_{\max} > 8 \text{ km s}^{-1}$ brings better agreement with the Local Group field halo results for the same V_{\max} selection criteria. The median WDM density profiles are then reduced relative to CDM by 60 per cent at all radii out to $r = 10 h^{-1} \text{ kpc}$, and the median WDM rotation curves show a more significant decrease of the order of $\sim 10 \text{ km s}^{-1}$. For the subhalo sets, we also find no significant difference in the L7, S229, and THM2 model subhalo internal properties. Similar to the Local Group field halo results, we find that, on average, the less massive the CDM subhalo, the greater reduction in the corresponding WDM density profile. Tidal stripping effects, however, can complicate a comparison of a single subhalo between CDM and WDM models.

Fig. 9 shows the V_{\max} relation between the Local Group field haloes in WDM and CDM. Haloes were selected by choosing Local Group CDM field haloes with a $V_{\max} > 8 \text{ km s}^{-1}$ and then identifying WDM halo counterparts that satisfy the halo correlation criterion described in Section 2. The orange curve shows the one-to-one correspondence between WDM and CDM. All Local Group WDM field haloes fall below the orange curve and show a trend

of increasingly smaller V_{\max} relative to the CDM values. The grey dashed curve in Fig. 9 shows a fit to the V_{\max} relation of

$$\frac{V_{\max}(\text{WDM})}{V_{\max}(\text{CDM})} = 1 - \left(\frac{V_{\max}(\text{CDM})}{V_0} \right)^\beta, \quad (4)$$

where $V_0 = 10.6 \text{ km s}^{-1}$ and $\beta = -1.58$ for all WDM haloes combined. The individual fits to the L7, S229, and THM2 models are not shown, but each is very similar to the combined fit. We note that V_{\max} values below $V_{\max} = 15 \text{ km s}^{-1}$ were included in order to obtain a more accurate accounting of the turnover in the $V_{\max, \text{WDM}} - V_{\max, \text{CDM}}$ relation. The $V_{\max, \text{WDM}} - V_{\max, \text{CDM}}$ relation summarizes the increased suppression of the WDM halo central density relative to CDM at smaller halo masses.

4 ABUNDANCE OF FIELD HALOES

The missing satellites and TBTF problems of CDM in the Local Group persist in the abundance and kinematics of field dwarf galaxies (Zavala et al. 2009; Klypin et al. 2015; Papastergis et al. 2015) motivating the exploration of non-linear evolution of WDM models in cosmological volumes. The redshift zero velocity functions of field DM haloes in a homogeneously resolved, $N_p = 512^3$ N -body simulation of a $L = 25 h^{-1} \text{ Mpc}$ box for the L7, S229, THM2 and CDM models are shown in Fig. 10. The CDM velocity function increases monotonically towards small mass down to $V_{\max} = 30 \text{ km s}^{-1}$. We calculate a power-law fit to the CDM velocity function, $dN/d \log V_{\max}$, that is based on the analytic approximation of Klypin et al. (2015) to the Bolshoi simulation results (Klypin, Trujillo-Gomez & Primack 2011). Our fit is very similar to the Klypin et al. (2015) fit with a power-law exponent of $n = -2.8$ and a ~ 20 per cent increase in the normalization. The analytic fit is shown in Fig. 10 to be in good agreement with the simulation results down to $V_{\max} = 30 \text{ km s}^{-1}$, below which numerical effects cause the CDM velocity function to turn over. The small differences we find in our fitting function with respect to Klypin et al. (2015) are reasonable given they result from different halo

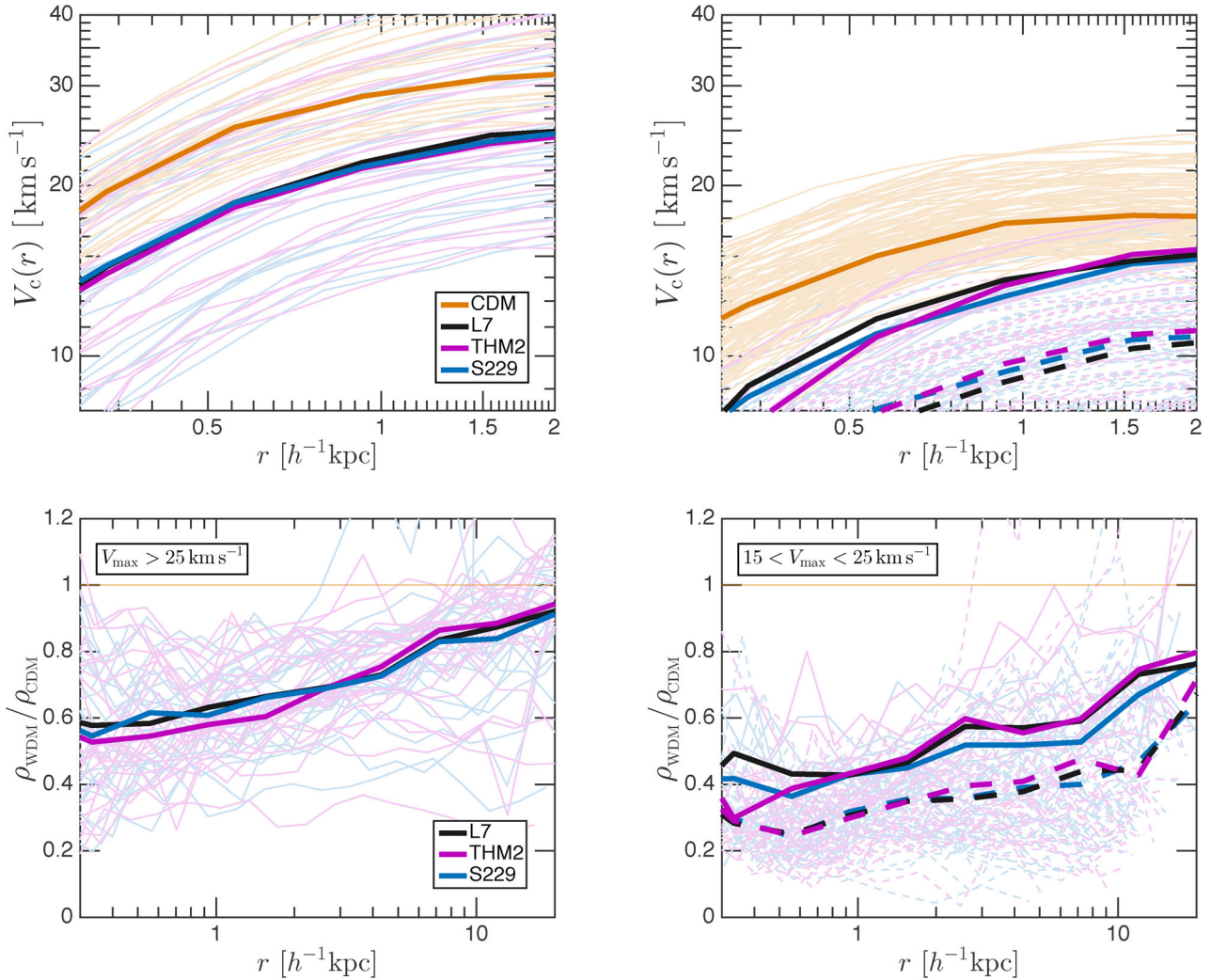


Figure 7. The rotation curves (top row) and density ratios (bottom row) of the Local Group field haloes for the CDM (orange), S229 (blue), and THM2 (magenta) DM models. The V_{\max} selection criteria for CDM haloes are labelled in the bottom row and explained in detail in the text. WDM field haloes with $V_{\max} > 15 \text{ km s}^{-1}$ are shown as solid curves and those with $8 < V_{\max} < 15 \text{ km s}^{-1}$ are dashed. The thick dark curves give the median values of each DM model halo set: solid for haloes with $V_{\max} > 15 \text{ km s}^{-1}$ and dashed for $V_{\max} > 8 \text{ km s}^{-1}$. The median relations of L7 haloes are shown in black (individual L7 halo curves are not shown for clarity). The WDM field haloes show a 40 per cent reduction in the median central density relative to CDM haloes with $V_{\max} > 25 \text{ km s}^{-1}$ (bottom-left panel), and a corresponding $\sim 5 \text{ km s}^{-1}$ reduction in the median rotation curves (top-left panel). Lower mass WDM haloes (right-hand panels) show a more pronounced decrease in the median density ratios of 60–70 per cent in the central $1 h^{-1} \text{ kpc}$ and 20–30 per cent near the haloes’ virial radius (although with significant scatter). Including WDM haloes with $8 < V_{\max} < 15 \text{ km s}^{-1}$ results in a more pronounced reduction in the WDM median density ratio and rotation curve relative to CDM.

finders analysing different simulations. The steepness of the velocity functions compound small differences in the determination of V_{\max} by different halo finders, where a ~ 7 per cent increase in the value of V_{\max} translates to a ~ 20 per cent increase in the normalization. Different halo finders applied to the same simulation return a 20–30 per cent variation in the cumulative velocity function, where the variation is primarily caused by the scatter in the mass determined for each individual halo (Knebe et al. 2011, 2013).

The L7, S229, and THM2 WDM model velocity functions agree with the CDM velocity function for larger mass haloes with $V_{\max} > 80 \text{ km s}^{-1}$, but are suppressed relative to CDM for low-mass haloes, reaching a factor of 2 suppression at $V_{\max} = 30 \text{ km s}^{-1}$. The sterile neutrino models and thermal WDM velocity functions agree with each other and an analytic fit to an $m = 2 \text{ keV}$ thermal WDM velocity function, where the equation is taken from Klypin et al. (2015)

and modified by our CDM power-law exponent and normalization values. The low-mass suppression in the WDM velocity function relative to CDM is related to the reduction in the WDM halo central density profiles found in the previous section and shown in Fig. 9. For haloes of the mass range considered here, the WDM haloes at a fixed abundance are the counterparts to CDM haloes of the same abundance, which corresponds to a leftward shift of the CDM velocity function to the WDM velocity function. However, at smaller masses below the resolution of these simulations, the suppression of structure formation in WDM models would become more prevalent, resulting in CDM haloes where a WDM counterpart does not form. This would correspond to a decrease in WDM halo abundance relative to CDM at fixed V_{\max} .

The ratio of the velocity functions between WDM and CDM models for field haloes at redshift $z = 6$ are shown in Fig. 11. We

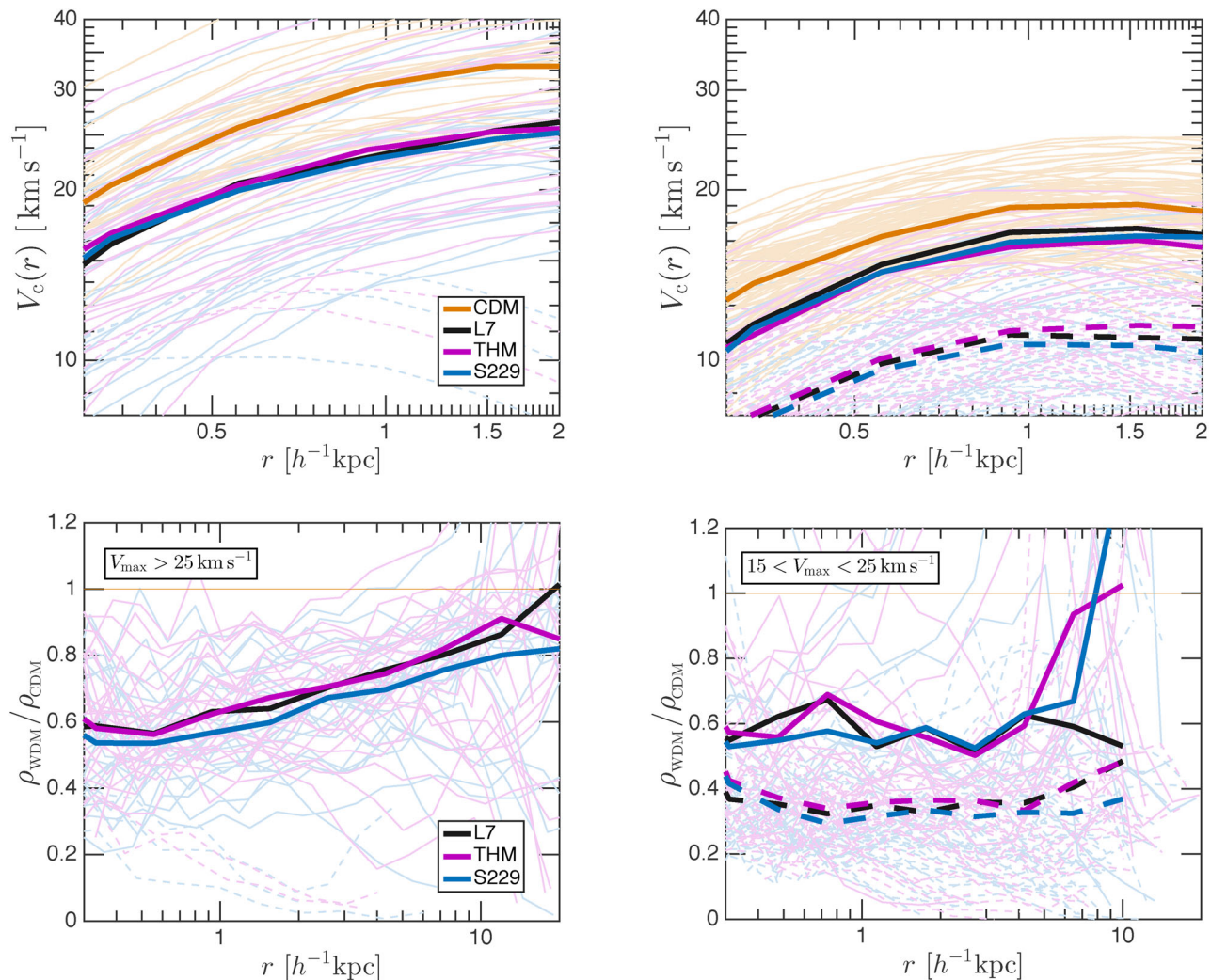


Figure 8. The rotation curves (top row) and density ratios (bottom row) of the Thelma and Louise subhaloes for the CDM (orange), S229 (blue), and THM2 (magenta) models. The same selection criteria and median curve styles as described in Fig. 7 are used, with the exception of the bottom-right panel, where the median density ratios are determined to $r < 10 h^{-1} \text{ kpc}$. The median rotation curves and density ratios of the $V_{\text{max}} > 25 \text{ km s}^{-1}$ subhaloes (left-hand column) are quantitatively similar to the Local Group field results shown in Fig. 7. The WDM subhaloes counterparts to CDM subhaloes with $15 < V_{\text{max}} < 25 \text{ km s}^{-1}$ (right-hand panels) show a 40 per cent reduction in the median central density relative to CDM, if only WDM subhaloes with $V_{\text{max}} > 15 \text{ km s}^{-1}$ are considered. There are only ~ 10 of these subhaloes in each set and there is considerable scatter around the median that is likely due to tidal stripping effects in both WDM and CDM subhaloes. Including WDM subhaloes with $V_{\text{max}} > 8 \text{ km s}^{-1}$ lowers the median density ratio and rotation curve relative to CDM, bringing them into better agreement with Local Group field halo results.

consider a broader range of models here. The velocity function ratios of all the A14 (solid curves) and V15 (dashed curves) sterile neutrino models and their thermal equivalent models (dot-dashed curves) are shown. The relative suppression between WDM and CDM abundances correlates with the warmth of the WDM models, as indicated by the convergence of the curves to three velocity function ratios at $V_{\text{max}} = 40 \text{ km s}^{-1}$ (with the exception of the S220 model). There are some variations between the velocity functions of the two sterile neutrino models and their thermal best-fitting model at intermediate scales between $45 \text{ km s}^{-1} < V_{\text{max}} < 60 \text{ km s}^{-1}$. This difference is on the 5–10 per cent level, and is likely not differentiable by future high-redshift galaxy surveys. It does suggest, however, that early stages of halo formation may have a relevant differences that could impact the quasi-linear regime, which we explore in the next section.

The agreement of abundances of field haloes in the thermal and sterile neutrino WDM models, where suppression of low-mass halo formation is significant relative to CDM, is similar to the abundance results of Local Group haloes shown in Fig. 5. Differences in the shape of the linear matter power spectrum between thermal and sterile neutrino WDM models are washed out in the deeply non-linear regime, even at high redshift.

5 QUASI-LINEAR REGIME

The progression from the significant differences between thermal WDM and resonantly produced sterile neutrino WDM models in the linear matter power spectrum, that sets the initial conditions for numerical simulations, to minimal observable differences in the non-linear measures we have explored at redshift zero motivates the

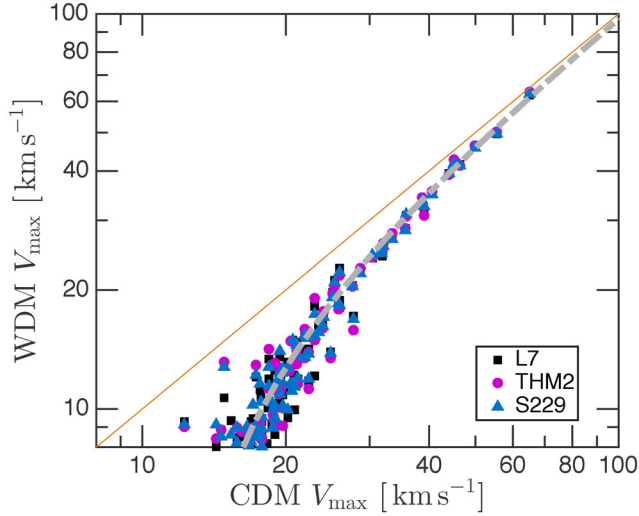


Figure 9. The WDM V_{\max} as a function of the matched CDM V_{\max} on a halo-by-halo basis for Local Group field haloes. The different WDM model haloes (L7 - black; S229 - blue; THM2 - magenta) have a similar distribution that bends away from the one-to-one relation (orange curve) with CDM haloes for smaller halo masses, as a result of reduced central densities in the WDM haloes. The grey curve shows a fit to the points that includes all WDM model haloes. Fits to individual WDM model halo sets (not shown) are similar to the fit for all WDM model haloes.

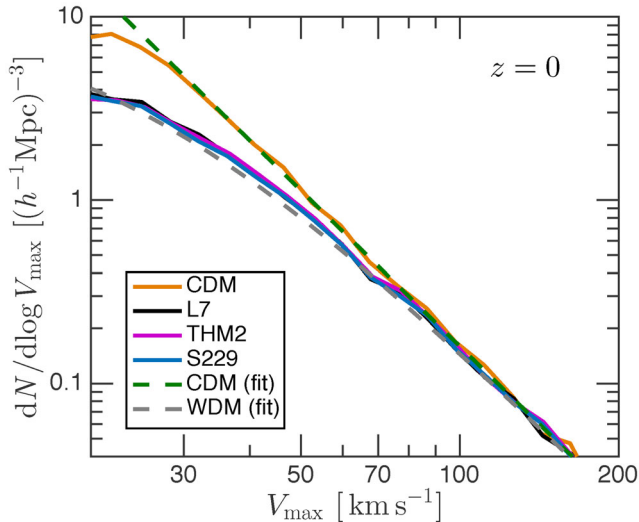


Figure 10. The circular velocity functions of field haloes in cosmological volume simulations for the CDM (orange), L7 (black), S229 (blue) and THM2 (magenta) DM models at redshift $z = 0$. The dashed green and grey curves, respectively, represent the CDM and thermal $m = 2$ keV WDM analytic approximations to the velocity functions. Our results show a good agreement with the analytic fits down to $V = 30$ km s $^{-1}$. The sterile neutrino and thermal WDM velocity functions are similar for the full range of halo masses and have a maximum suppression of a factor of 2 relative to low-mass CDM halo abundances.

study of an intermediate, quasi-linear regime. We consider growth of structure in the quasi-linear regime by determining the 3D non-linear matter power spectrum of the homogeneously resolved cosmological simulations at $z \sim 3-6$ described in the previous section. Viel et al. (2012) did convergence testing for N -body simulations with the same cosmology, simulation box size, and number of par-

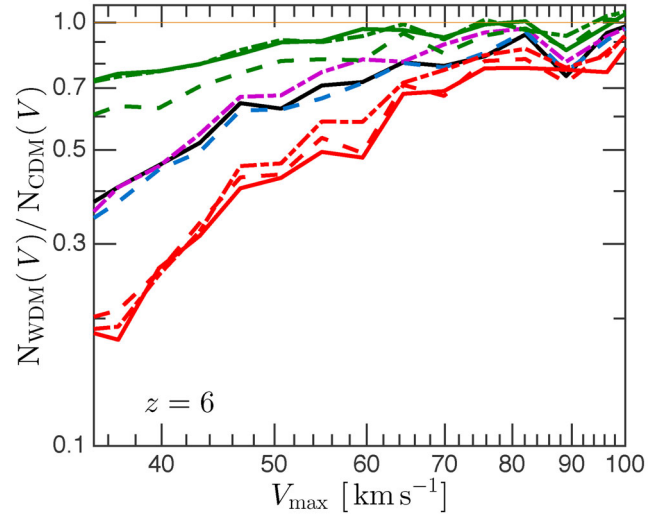


Figure 11. The ratio of the circular velocity functions of WDM models to CDM for field haloes at a redshift of $z = 6$. The WDM models shown: L46 (solid; green), S220 (dashed; green), THM2.9 (dash-dotted; green), L7 (solid; black), S229 (dashed; blue), THM2 (dash-dotted; magenta), L48 (solid; red), S208 (dashed; red), THM1.6 (dash-dotted; red). The WDM model velocity function ratios cluster into three groups according to their respective warmth, with only a small 5–10 per cent variation in the velocity function ratios between WDM models of comparable warmth.

ticles, and found their power spectra converged to $k = 50 h \text{Mpc}^{-1}$. We therefore set $k = 50 h \text{Mpc}^{-1}$ as our limiting scale.

Fig. 12 shows the ratio of each WDM model’s matter power spectrum to the CDM matter power spectrum at redshift $z = 2.98$ (solid) and $z = 5.429$ (dashed) in the left-hand column. Each row in Fig. 12 gives the results for a set of WDM models of comparable warmth that includes two sterile neutrino models (one for each V15 and A14) and their thermal equivalent WDM model. The thin, solid curves in each panel of the left-hand column show the linear matter power spectrum ratios for each WDM model relative to CDM. By redshift $z = 5.429$, the non-linear matter power spectrum calculated from the simulations have diverged from the linear matter power spectrum by at least a few per cent at $k = 5 h \text{Mpc}^{-1}$ for all but the coldest WDM models (top-left panel), and all WDM models show significant evolution from the linear matter power spectrum on scales of $k = 10 h \text{Mpc}^{-1}$. Viel et al. (2013) find that a few per cent suppression in the $m = 2$ keV thermal WDM 3D non-linear matter power spectrum relative to CDM at $k = 10 h \text{Mpc}^{-1}$ is differentiable in the Lyman- α forest 1D flux power spectrum at these redshifts. The scales and the degree of power spectrum suppression of the sterile neutrino models relative to CDM that we find here is, therefore, relevant for Lyman- α forest measurements (Viel et al. 2012, 2013).

The right-hand column of Fig. 12 shows the power spectrum ratios of the sterile neutrino models with respect to the matter power spectrum of the equivalent thermal WDM model for $z = 2.98$ (solid) and $z = 5.429$ (dashed). The S229 and S208 model power spectrum ratios show similar departures from thermal WDM for $k > 2 h \text{Mpc}^{-1}$ at both $z = 2.98$ and 5.429. Compared to these two warmer V15 models, the S220 model (top-right panel) has a slightly greater reduction in power spectrum relative to thermal WDM at $k = 50 h \text{Mpc}^{-1}$. The A14 models show a greater variation in the power spectrum ratios with their thermal equivalent models than the qualitatively uniform V15 models. The coldest A14 model, L46, is consistent with its thermal equivalent on all scales and redshifts.

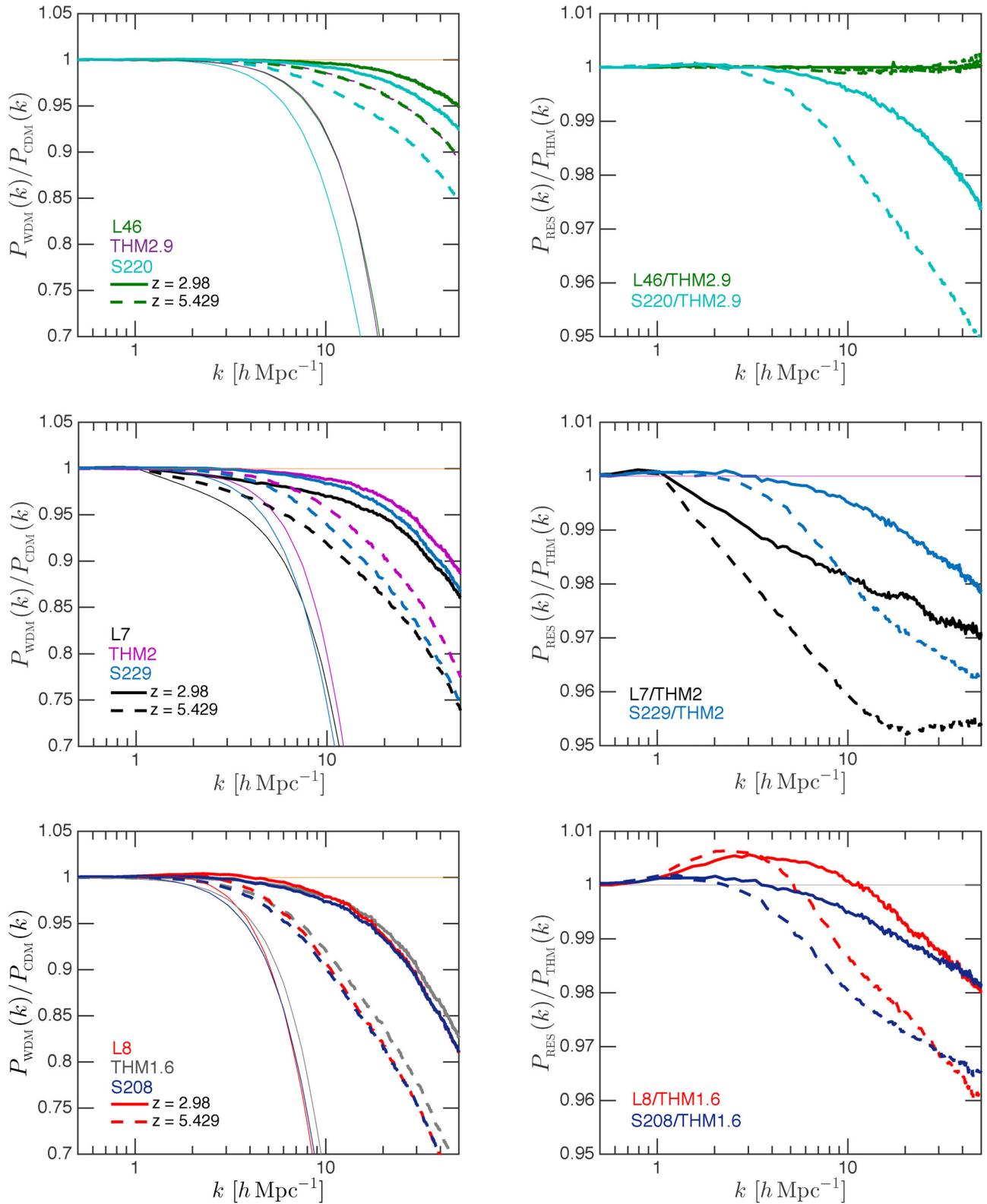


Figure 12. Left-hand column: ratio of the 3D matter power spectrum for WDM models with respect to CDM for redshifts $z = 2.98$ (solid) and $z = 5.429$ (dashed). Right-hand column: ratio of the 3D matter power spectrum of sterile neutrino models with respect to a thermal equivalent WDM model. Rows divide WDM models into groups of similar model warmth. Top row: L46 (green), S220 (cyan), THM2.9 (purple). Middle row: L7 (black), S229 (blue), and THM2 (magenta). Bottom row: L8 (red), S208 (blue), THM1.6 (grey). Solid, thin curves (left-hand column) are the linear matter power spectrum ratios of WDM to CDM. The 3D matter power spectrum of the sterile neutrino and thermal WDM models suppress small-scale power relative to CDM, but to differing degrees depending on the warmth of the model. The matter power spectrum ratios on scales above $k > 1 \text{ h Mpc}^{-1}$ show differences at the few per cent level, which is significant, between the sterile neutrino and thermal WDM models.

The L7 model (middle-right panel) shows suppression relative to the power spectrum of the $m = 2$ keV thermal WDM model for scales $k > 1 h \text{Mpc}^{-1}$. The warmest A14 model, L8 (shown in the bottom-right panel), has more power relative to thermal WDM for $1 < k < 5(10) h \text{Mpc}^{-1}$ at $z = 5.429$ (2.98), and increasingly less power than thermal WDM on smaller scales.

The relative strength of the resonant sterile neutrino matter power spectrum at a fixed scale compared to a thermal equivalent WDM model does not correlate with warmth or the details of the resonant sterile neutrino production calculation, i.e. V15 and A14 models. For example, the L7 model shows enhanced suppression relative to the S229 model, but the L8 model has more power than the S208 model for $k < 50 h \text{Mpc}^{-1}$. The detailed shape of transfer function is, therefore, the most relevant parameter for determining the relative power in the quasi-linear regime for the scales probed here.

A direct comparison with measurements of the Lyman- α forest is beyond the scope of this paper. However, if a few per cent difference in the 3D non-linear matter power for $k = 10 h \text{Mpc}^{-1}$ at $z = 3-5$ can distinguish thermal WDM from CDM, as claimed (Viel et al. 2012, 2013), then the percent level differences of sterile neutrino models from thermal WDM that we find here are significant. A full Lyman- α study should then be able to differentiate between sterile neutrino models and a thermal equivalent model, where non-linear matter power spectrums differ at a few per cent level on scales above the half-mode suppression scale. Constraints on WDM particle masses for models with non-thermal distributions, such as sterile neutrinos, from thermal WDM tests are therefore inadequate. Future Lyman- α observations that can probe scales of $10 < k < 50 h \text{Mpc}^{-1}$ would have great ability to test these models further.

6 DISCUSSION AND CONCLUSIONS

In this paper, we have presented a variety of simulations – both zoom-ins of Local Group analogues and homogeneously resolved cosmological volumes – of sterile neutrino DM. The focus of our work is on resonantly produced sterile neutrinos, which result in transfer functions that differ significantly from the standard assumption of a thermal relic. We use transfer functions from both A14 and V15, the latter being a more accurate calculation of the former, and best-fitting thermal WDM approximations. This allows a detailed exploration of transfer function shape on Local Group halo properties while evaluating the resonant sterile neutrino models that are best able to explain the 3.55 keV anomalous X-ray signal found by various surveys (Boyarsky et al. 2014; Bulbul et al. 2014).

We find the density profiles, shapes, and mass assembly histories of the Local Group host halo pairs are similar for all DM models, irrespective of the warmth of the WDM model. The abundance of low-mass subhaloes in each WDM host is reduced significantly relative to CDM and depends on the warmth of the model. The reduction in the number of low-mass subhaloes alleviates the missing satellites problem. However, the number of Local Group subhaloes could also be used to rule out these and similar sterile neutrino models if the number of MW and M31 satellite galaxies exceeds the predicted number of WDM haloes. This depends on the total number of dwarf galaxies found by future surveys (Tollerud et al. 2008; Hargis, Willman & Peter 2014) and the minimum DM halo mass that would host a detectable satellite galaxy (Koposov et al. 2008; Polisensky & Ricotti 2011; Kennedy et al. 2014; Horiuchi et al. 2014). The abundance of subhaloes at the resolution limit of the warmest sterile neutrino model considered here, L8, is near the current satellite count for both the MW and M31 and could be

ruled out in the near future by DES, LSST or WFIRST (Ivezic et al. 2008; Bechtol et al. 2015; Spergel et al. 2015). The abundance of low-mass field haloes is also suppressed relative to CDM, with a suppression that is well described by the thermal-equivalent mass of the WDM model.

The internal properties of WDM Local Group field haloes and MW/M31 subhaloes also show differences relative to their CDM counterparts: the WDM haloes have a reduced central density that becomes more pronounced for lower halo masses. However, even WDM haloes several times more massive than the WDM model half-mode mass, below which free-streaming effects are typically considered most relevant, show a 40 per cent decrease, on average, in their central density relative to CDM. A similar result was found for subhaloes in thermal WDM simulations of MW-sized DM hosts (Polisensky & Ricotti 2014; Schneider et al. 2014) and field haloes in simulations using thermal approximations to resonant sterile neutrino WDM models (Bose et al. 2016). This is unsurprising, as we find the median density profile ratios and rotation curves do not show any significant variation between thermal and resonant sterile neutrino WDM models.

Importantly, we find that the half-mode mass is largely predictive of the number of Local Group haloes, the abundance of low-mass haloes in the field, and for the density reduction in WDM haloes relative to CDM. For the range of scales probed here, non-linear evolution washes away linear matter power spectrum differences other than overall suppression of small-scale power that is effectively captured by a single parameter, the half-mode mass. However, the more accurate resonant sterile neutrino transfer function should be used when testing sterile neutrino models with observed satellite galaxy counts, as differences at the 10 per cent level may persist and are important in constraining DM models via the luminosity function of Local Group satellites (Horiuchi et al. 2016).

At high redshift, in the quasi-linear regime on scales that are relevant for Lyman- α forest measurements, we find quantitative differences in the 3D matter power spectrum of resonantly produced sterile neutrino and thermal WDM models. The differences in the linear matter power spectrum between the resonant sterile neutrino DM models (based on two separate calculations by V15 and A14) and their thermal equivalent WDM model are preserved in the redshift $z = 3-5$ matter power spectrum of these models at a few per cent level on small scales. The 3D matter power spectrum differences found here could translate into relevant differences in the Lyman- α forest 1D flux power spectrum (Viel et al. 2013). Measurements in the Lyman- α forest may be able to discern between structure formation resulting from different sterile neutrino DM models and thermal WDM models before the epoch where non-linear evolution washes away differences in the linear matter power spectrum.

We find that the exact transfer function shape is important for placing constraints on resonantly produced sterile neutrino WDM models. Thermal WDM approximations are sufficient for some studies, such as the internal properties of Local Group haloes, and abundance of haloes in the Local Group or large cosmological volumes. However, careful consideration should be given when comparing Local Group luminosity functions to subhalo mass functions (Horiuchi et al. 2016) and when comparing 3D matter power spectrum results from cosmological volume simulations to Lyman- α forest measurements. Simple extrapolations of constraints from thermal WDM studies to resonantly produced sterile neutrino DM models have been shown here to be incorrect. Future surveys of the Local Group by LSST, DES, and WFIRST, as well as detailed studies of the Lyman- α forest that consider scales in the quasi-linear regime, have great power to test resonant sterile neutrino models.

ACKNOWLEDGEMENTS

We thank Tejaswi Venumadhav and Francis-Yan Cyr-Racine for useful discussions. The authors acknowledge the University of Maryland supercomputing resources (<http://www.it.umd.edu/hpcc>) made available for conducting the research reported in this paper. MBK acknowledges support from NASA through Hubble Space Telescope theory grants (programmes AR-12836 and AR-13888) from the Space Telescope Science Institute (STScI), which is operated by the Association of Universities for Research in Astronomy (AURA), Inc., under NASA contract NAS5-26555. Support for SGK was provided by NASA through *Einstein* Postdoctoral Fellowship grant number PF5-160136 awarded by the *Chandra* X-ray Center, which is operated by the Smithsonian Astrophysical Observatory for NASA under contract NAS8-03060. KNA is partially supported by NSF CAREER Grant no. PHY-11-59224 and NSF Grant no. PHY-1316792.

REFERENCES

- Abazajian K., 2006, *Phys. Rev. D*, 73, 063506
 Abazajian K. N., 2014, *Phys. Rev. Lett.*, 112, 161303 (A14)
 Abazajian K. N., Fuller G. M., 2002, *Phys. Rev. D*, 66, 023526
 Anderhalden D., Diemand J., Bertone G., Macciò A. V., Schneider A., 2012, *J. Cosmol. Astropart. Phys.*, 10, 47
 Anderhalden D., Schneider A., Macciò A. V., Diemand J., Bertone G., 2013, *J. Cosmol. Astropart. Phys.*, 3, 14
 Asaka T., Blanchet S., Shaposhnikov M., 2005, *Phys. Lett. B*, 631, 151
 Avila-Reese V., Colín P., Valenzuela O., D’Onghia E., Firmani C., 2001, *ApJ*, 559, 516
 Baur J., Palanque-DeLabrouille N., Yèche C., Magneville C., Viel M., 2015, preprint ([arXiv:1512.01981](https://arxiv.org/abs/1512.01981))
 Bechtol K. et al., 2015, *ApJ*, 807, 50
 Bode P., Ostriker J. P., Turok N., 2001, *ApJ*, 556, 93
 Bose S., Hellwing W. A., Frenk C. S., Jenkins A., Lovell M. R., Helly J. C., Li B., 2016, *MNRAS*, 455, 318
 Boyarsky A., Lesgourgues J., Ruchayskiy O., Viel M., 2009, *J. Cosmol. Astropart. Phys.*, 5, 012
 Boyarsky A., Ruchayskiy O., Iakubovskiy D., Franse J., 2014, *Phys. Rev. Lett.*, 113, 251301
 Boyarsky A., Franse J., Iakubovskiy D., Ruchayskiy O., 2015, *Phys. Rev. Lett.*, 115, 161301
 Boylan-Kolchin M., Bullock J. S., Kaplinghat M., 2011, *MNRAS*, 415, L40
 Boylan-Kolchin M., Bullock J. S., Kaplinghat M., 2012, *MNRAS*, 422, 1203
 Brook C. B. et al., 2011, *MNRAS*, 415, 1051
 Buckley M. R., Zavala J., Cyr-Racine F.-Y., Sigurdson K., Vogelsberger M., 2014, *Phys. Rev. D*, 90, 043524
 Bulbul E., Markevitch M., Foster A., Smith R. K., Loewenstein M., Randall S. W., 2014, *ApJ*, 789, 13
 Bullock J. S., Kravtsov A. V., Weinberg D. H., 2000, *ApJ*, 539, 517
 Boehm C., Schewtschenko J. A., Wilkinson R. J., Baugh C. M., Pascoli S., 2014, *MNRAS*, 445, L31
 Colín P., Valenzuela O., Avila-Reese V., 2008, *ApJ*, 673, 203
 Colombi S., Dodelson S., Widrow L. M., 1996, *ApJ*, 458, 1
 de Gouvêa A., 2005, *Phys. Rev. D*, 72, 033005
 di Cintio A., Knebe A., Libeskind N. I., Yepes G., Gottlöber S., Hoffman Y., 2011, *MNRAS*, 417, L74
 Di Cintio A., Brook C. B., Macciò A. V., Stinson G. S., Knebe A., Dutton A. A., Wadsley J., 2014, *MNRAS*, 437, 415
 Dodelson S., Widrow L. M., 1994, *Phys. Rev. Lett.*, 72, 17
 Dunstan R. M., Abazajian K. N., Polisensky E., Ricotti M., 2011, preprint ([arXiv:1109.6291](https://arxiv.org/abs/1109.6291))
 Flores R. A., Primack J. R., 1994, *ApJ*, 427, L1
 Frenk C. S., White S. D. M., 2012, *Ann. Phys., Lpz.*, 524, 507
 Garrison-Kimmel S., Rocha M., Boylan-Kolchin M., Bullock J. S., Lally J., 2013, *MNRAS*, 433, 3539
 Garrison-Kimmel S., Boylan-Kolchin M., Bullock J. S., Lee K., 2014a, *MNRAS*, 438, 2578
 Garrison-Kimmel S., Boylan-Kolchin M., Bullock J. S., Kirby E. N., 2014b, *MNRAS*, 444, 222
 Governato F. et al., 2010, *Nature*, 463, 203
 Governato F. et al., 2012, *MNRAS*, 422, 1231
 Hahn O., Abel T., 2011, *MNRAS*, 415, 2101
 Hargis J. R., Willman B., Peter A. H. G., 2014, *ApJ*, 795, L13
 Horiuchi S., Humphrey P. J., Oñorbe J., Abazajian K. N., Kaplinghat M., Garrison-Kimmel S., 2014, *Phys. Rev. D*, 89, 025017
 Horiuchi S., Bozek B., Abazajian K. N., Boylan-Kolchin M., Bullock J. S., Garrison-Kimmel S., Oñorbe J., 2016, *MNRAS*, 456, 4346
 Iakubovskiy D., Bulbul E., Foster A. R., Savchenko D., Sadova V., 2015, preprint ([arXiv:1508.05186](https://arxiv.org/abs/1508.05186))
 Ivezić Z. et al., 2008, preprint ([arXiv:0805.2366](https://arxiv.org/abs/0805.2366))
 Kennedy R., Frenk C., Cole S., Benson A., 2014, *MNRAS*, 442, 2487
 Kirby E. N., Bullock J. S., Boylan-Kolchin M., Kaplinghat M., Cohen J. G., 2014, *MNRAS*, 439, 1015
 Klypin A., Kravtsov A. V., Valenzuela O., Prada F., 1999, *ApJ*, 522, 82
 Klypin A. A., Trujillo-Gomez S., Primack J., 2011, *ApJ*, 740, 102
 Klypin A., Karachentsev I., Makarov D., Nasonova O., 2015, *MNRAS*, 454, 1798
 Knebe A. et al., 2011, *MNRAS*, 415, 2293
 Knebe A. et al., 2013, *MNRAS*, 435, 1618
 Knollmann S. R., Knebe A., 2009, *ApJS*, 182, 608
 Koposov S. et al., 2008, *ApJ*, 686, 279
 Kravtsov A. V., Gnedin O. Y., Klypin A. A., 2004, *ApJ*, 609, 482
 Larson D. et al., 2011, *ApJS*, 192, 16
 Lovell M. R. et al., 2012, *MNRAS*, 420, 2318
 Lovell M. R., Frenk C. S., Eke V. R., Jenkins A., Gao L., Theuns T., 2014, *MNRAS*, 439, 300
 Macciò A. V., Paduroiu S., Anderhalden D., Schneider A., Moore B., 2012, *MNRAS*, 424, 1105
 McConnachie A. W., 2012, *AJ*, 144, 4
 Marsh D. J. E., Pop A.-R., 2015, *MNRAS*, 451, 2479
 Marsh D. J. E., Silk J., 2014, *MNRAS*, 437, 2652
 Moore B., 1994, *Nature*, 370, 629
 Moore B., Ghigna S., Governato F., Lake G., Quinn T., Stadel J., Tozzi P., 1999, *ApJ*, 524, L19
 Obreschkow D., Power C., Bruderer M., Bonvin C., 2013, *ApJ*, 762, 115
 Oñorbe J., Boylan-Kolchin M., Bullock J. S., Hopkins P. F., Kereš D., Faucher-Giguère C.-A., Quataert E., Murray N., 2015, *MNRAS*, 454, 2092
 Papastergis E., Giovanelli R., Haynes M. P., Shankar F., 2015, *A&A*, 574, A113
 Patwardhan A. V., Fuller G. M., Kishimoto C. T., Kusenko A., 2015, *Phys. Rev. D*, 92, 103509
 Peñarrubia J., Pontzen A., Walker M. G., Koposov S. E., 2012, *ApJ*, 759, L42
 Polisensky E., Ricotti M., 2011, *Phys. Rev. D*, 83, 043506
 Polisensky E., Ricotti M., 2014, *MNRAS*, 437, 2922
 Power C., Navarro J. F., Jenkins A., Frenk C. S., White S. D. M., Springel V., Stadel J., Quinn T., 2003, *MNRAS*, 338, 14
 Primack J. R., 2015, preprint ([arXiv:1505.02821](https://arxiv.org/abs/1505.02821))
 Rocha M., Peter A. H. G., Bullock J. S., Kaplinghat M., Garrison-Kimmel S., Oñorbe J., Moustakas L. A., 2013, *MNRAS*, 430, 81
 Schneider A., 2015, *MNRAS*, 451, 3117
 Schneider A., Smith R. E., Macciò A. V., Moore B., 2012, *MNRAS*, 424, 684
 Schneider A., Anderhalden D., Macciò A. V., Diemand J., 2014, *MNRAS*, 441, L6
 Shao S., Gao L., Theuns T., Frenk C. S., 2013, *MNRAS*, 430, 2346
 Shi X., Fuller G. M., 1999, *Phys. Rev. Lett.*, 82, 2832
 Spergel D. et al., 2015, preprint ([arXiv:1503.03757](https://arxiv.org/abs/1503.03757))
 Springel V., 2005, *MNRAS*, 364, 1105
 Tollerud E. J., Bullock J. S., Strigari L. E., Willman B., 2008, *ApJ*, 688, 277
 Tollerud E. J., Boylan-Kolchin M., Bullock J. S., 2014, *MNRAS*, 440, 3511

- van der Marel R. P., Fardal M., Besla G., Beaton R. L., Sohn S. T., Anderson J., Brown T., Guhathakurta P., 2012, *ApJ*, 753, 8
- Venumadhav T., Cyr-Racine F.-Y., Abazajian K. N., Hirata C. M., 2015, preprint ([arXiv:1507.06655](https://arxiv.org/abs/1507.06655)) (V15)
- Vera-Ciro C. A., Helmi A., Starkenburg E., Breddels M. A., 2013, *MNRAS*, 428, 1696
- Viel M., Lesgourgues J., Haehnelt M. G., Matarrese S., Riotto A., 2005, *Phys. Rev. D*, 71, 063534
- Viel M., Markovič K., Baldi M., Weller J., 2012, *MNRAS*, 421, 50
- Viel M., Becker G. D., Bolton J. S., Haehnelt M. G., 2013, *Phys. Rev. D*, 88, 043502
- Vogelsberger M., Zavala J., Loeb A., 2012, *MNRAS*, 423, 3740
- Wang J., White S. D. M., 2007, *MNRAS*, 380, 93
- Wang J., Frenk C. S., Navarro J. F., Gao L., Sawala T., 2012, *MNRAS*, 424, 2715
- Wang M.-Y., Peter A. H. G., Strigari L. E., Zentner A. R., Arant B., Garrison-Kimmel S., Rocha M., 2014, *MNRAS*, 445, 614
- Zavala J., Jing Y. P., Faltenbacher A., Yepes G., Hoffman Y., Gottlöber S., Catinella B., 2009, *ApJ*, 700, 1779
- Zolotov A. et al., 2012, *ApJ*, 761, 71

This paper has been typeset from a $\text{T}_{\text{E}}\text{X}/\text{L}^{\text{A}}\text{T}_{\text{E}}\text{X}$ file prepared by the author.